

# Long-term stable nonlinear evolutions of ultracompact black-hole mimickers

Gareth Arturo Marks <sup>1,\*</sup> Seppe J. Staelens <sup>1,2,†</sup> Tamara Evstafyeva <sup>3,‡</sup> and Ulrich Sperhake <sup>1,4,5,§</sup>

<sup>1</sup>*DAMTP, Centre for Mathematical Sciences, University of Cambridge, Wilberforce Road, Cambridge CB3 0WA, UK*

<sup>2</sup>*Leuven Gravity Institute, KU Leuven, Celestijnenlaan 200D box 2415, 3001 Leuven, Belgium*

<sup>3</sup>*Perimeter Institute for Theoretical Physics, Waterloo, Ontario N2L 2Y5, Canada*

<sup>4</sup>*Department of Physics and Astronomy, Johns Hopkins University,  
3400 North Charles Street, Baltimore, Maryland 21218, USA*

<sup>5</sup>*TAPIR 350-17, Caltech, 1200 E. California Boulevard, Pasadena, California 91125, USA*

(Dated: April 25, 2025)

We study the stability of ultracompact boson stars admitting light rings combining a perturbative analysis with 3+1 numerical-relativity simulations with and without symmetry assumptions. We observe excellent agreement between all perturbative and numerical results which uniformly support the hypothesis that this family of black-hole mimickers is separated into stable and unstable branches by extremal-mass configurations. This separation includes, in particular, thin-shell boson stars with light rings located on the stable branch which we conclude to represent long-term stable black-hole mimickers.

## I. INTRODUCTION

Black-hole solutions in closed analytic form have played a crucial role in many aspects of the theoretical understanding of general relativity (GR) almost right from the moment Einstein published his theory. Starting with observations of X-ray sources (e.g. Cygnus X-1 [1]) and quasars (e.g. 3C 273 [2, 3]), and their eventual identification with accretion onto compact objects, black holes (BHs) acquired an equally prominent role as seemingly common citizens of our universe. The rapidly increasing number of gravitational-wave (GW) detections by LIGO and Virgo [4, 5], all compatible with theoretical predictions for BHs and neutron stars in GR [6], and direct observations of BH shadows by the Event Horizon Telescope [7, 8] has further cemented the prominence of BHs in observational astronomy.

In both mathematical modeling as well as popular imagination, the most characteristic feature of a BH is its event horizon, the boundary of an interior region from which nothing, not even light, can escape. In terms of their observational phenomenology, however, the decisive feature of BHs are their (unstable) light rings (LRs), circular null-geodesics on which photons can orbit; for a Schwarzschild BH of mass  $M$ , the event horizon is located at areal radius  $r = 2GM/c^2$  and the LR at  $r = 3GM/c^2$ . The shape of BH shadows, accretion dynamics and the BH ringdown spectrum are closely related to LRs and the perturbational potential in their vicinity [9–12]. The observational evidence therefore points more directly at the existence of LRs, not necessarily BHs. Additionally, classical black holes come with theoretical problems, like the singularity and the information paradox [13], motivating the study of BH mimickers. The GW emission

from compact boson-star (BS) binaries furthermore exhibits significant degeneracy with that from BH binaries [14]. Even if one accepts Occam’s razor and parsimoniously interprets BHs as the most likely sources, there remains the intriguing possibility that a population of ultra-compact objects (UCOs) is hiding inside a more conventional BH society and may provide us with clues about dark-matter candidate fields they are composed of.

Clearly, dynamical longevity is a key requirement of any viable alternative to the BH paradigm. The stability of UCOs or *BH mimickers* – both implied henceforth to denote objects with a LR but no horizon – has, consequently, gained much attention in recent years. Under a broad set of assumptions, BH mimickers have been shown to possess two LRs, one stable and one unstable located at the minimum and maximum, respectively, of the null geodesic’s potential [15, 16]; Kerr BHs, in contrast only have unstable LRs. The existence of a minimum in the effective potential leads to *stable trapping*, i.e. null geodesics originating close to the minimum may remain indefinitely bound to it. At linear level, waves propagating on a background spacetime with stable trapping exhibit decay slower than polynomial or exponential as occurs for unstable trapping [17]. Guided by results on the instability of anti-de Sitter spacetime and its similar decay rates [18–20], it has been heuristically argued that UCOs may also be nonlinearly unstable, thereby ruling them out as plausible BH mimickers [21]. In the absence of rigorous analytic results, however, numerical evolutions are the only available tool for testing this hypothesis.

To date, literature results investigating the ultimate fate and stability of UCOs are inconclusive. By simulating two families of ultracompact BSs, Ref. [22] either finds migration to nonultracompact configurations or collapse to a BH, typically on timescales  $\lesssim \mathcal{O}(10^3) \mu^{-1}$  in units of the scalar mass parameter, and concludes that the LRs trigger instability. Reference [23] explains the instability as the result of the backreaction of perturbations at the stable LR appearing to deepen the geodesic po-

\* gam54@cam.ac.uk

† ss3033@cam.ac.uk

‡ tevstafyeva@perimeterinstitute.ca

§ U.Sperhake@damtp.cam.ac.uk

tential. In contrast, simulations of the merger and ring-down of ultracompact spinning BSs yield no evidence of this instability [24], although the timescales the simulations span in that work are considerably shorter. Further simulations in spherical symmetry of scalarized Reissner-Nordström BHs with LRs also exhibited long-term stability [25]. In a recent study using a toy-model spacetime with two LRs, Ref. [26] analyzes the differences between linear and non-linear dynamics in more detail: within the region of stable trapping, the slow linear decay leads to a growth of higher-order derivatives and energy in the nonlinear evolution, thereby resulting in turbulent behaviour. This phenomenon is proven in the perturbative regime [27], where the authors argue how it may not necessarily trigger an instability. The ultimate end state of these configurations, however, remains an open question.

Here, we explore the stability of a class of spherically symmetric ultracompact BSs with LRs, characterized by *thin-shell* profiles [28] and reaching compactness  $C \sim 0.32$ . We combine a set of numerical simulations in spherical symmetry (1+1), axisymmetry (2+1) and full 3+1 dimensions with perturbative calculations of the radial oscillation frequency, observing excellent agreement between all approaches compatible with the standard result that stable and unstable branches of stars, including UCOs with LRs, are separated by local extrema in the mass-radius diagram. In particular, we observe no signs of instability on the stable branch containing BH mimickers in agreement with the restabilization, i.e. real frequency, of the fundamental radial oscillation mode predicted in this regime by our perturbative calculations.

The paper is organised as follows. Sec. II presents the BS models considered, as well as the different codes. Sec. III summarizes our evolutions, showcasing their stability. We connect the observed dynamics to linear perturbation theory in Sec. IV, and demonstrate that the light ring structure is preserved in Sec. V. We supplement our detailed evolutions with a wider range of models in Sec. VI, before concluding in Sec. VII. Henceforth, we employ Planck units  $c = G = \hbar = 1$ , but keep the scalar-field mass parameter  $\mu$  which controls the scale invariance of the spacetimes in question. Code units are translated into SI (or similar) by fixing  $\mu$  and scaling with appropriate powers thereof: e.g.  $\mu = 1.33 \times 10^{-10}$  eV corresponds to  $\mu^{-1} = M_{\odot} = 1.48$  km.

## II. THEORY AND NUMERICAL CODES

We consider BSs in GR composed of one complex scalar field  $\varphi$  with solitonic potential  $V(\varphi)$  minimally coupled to gravity by the action

$$S = \int \sqrt{-g} \left\{ \frac{R}{16\pi} - \frac{1}{2} [g^{\mu\nu} \nabla_{\mu} \bar{\varphi} \nabla_{\nu} \varphi + V(\varphi)] \right\} d^4x, \quad (1)$$

$$V(\varphi) = \mu^2 |\varphi|^2 \left( 1 - 2 \frac{|\varphi|^2}{\sigma_0^2} \right)^2, \quad \sigma_0 = \text{const.}$$

TABLE I. Nickname, solitonic potential parameter  $\sigma_0$ , central scalar-field amplitude  $A_0$ , ADM mass  $M$ , Noether charge  $\mathcal{N}$ , the radius  $r_{99}$  encompassing 99% of the total mass, compactness  $C$  and fundamental radial oscillation frequency  $\chi_0^2$  for the two BS models marked by square and circle in Fig. 1.

Model	$\sigma_0$	$A_0$	$\mu M$	$\mu^2 \mathcal{N}$	$\mu r_{99}$	$C$	$\chi_0^2 / \mu^2$
S06A044	0.06	0.044	10.43	65.9	31.7	0.33	$7.52 \times 10^{-5}$
S08A06	0.08	0.06	5.65	26.1	17.9	0.31	$2.68 \times 10^{-5}$

Varying  $S$  results in the Einstein-Klein-Gordon equations

$$G_{\alpha\beta} = 8\pi T_{\alpha\beta}, \quad \nabla^{\mu} \nabla_{\mu} \varphi = \frac{dV}{d\varphi}, \quad (2)$$

$$T_{\mu\nu} = \frac{1}{2} \nabla_{(\mu} \bar{\varphi} \nabla_{\nu)} \varphi - \frac{g_{\mu\nu}}{2} [g^{\alpha\beta} \nabla_{\alpha} \bar{\varphi} \nabla_{\beta} \varphi + V(\varphi)].$$

We compute stationary BS models in spherical symmetry writing  $\varphi(t, r) = A(r)e^{i\omega t}$  and using a GR version with quadruple-precision of the two-way shooting code of Ref. [29]. The resulting single-BS spacetimes are evolved in time using four different codes in spherical symmetry, axisymmetry or full 3D using the Baumgarte-Shapiro-Shibata-Nakamura (BSSN) [30, 31] and the conformal covariant Z4 (CCZ4) [32] formulations. (i) SPHERICALBSEVOLVER achieves spherically symmetry time evolutions through dimensional reduction with  $SO(3)$  symmetry according to Ref. [33] using a uniform radial grid. (ii) A 2D code implements axisymmetry using the same modified cartoon method but for  $SO(2)$  isometry. It is based on (iii) EXOZVEZDA [34], a code for exotic matter built on GRCHOMBO [35, 36], which evolves 3D domains with adaptive mesh refinement provided by CHOMBO [37]. (iv) LEAN [38] is based on the CACTUS computational toolkit [39] and evolves 3D domains with mesh refinement provided by CARPET [40]. In the following, we will refer to these codes and their respective simulations with the acronyms **Sph**, **Axi**, **E3D** and **L3D**. Unless specified otherwise, our simulations employ a resolution  $h = 1/(12\mu)$  with outer boundary at  $256\mu^{-1}$  on a unigrid (**Sph**) or using 5 refinement levels (**Axi**, **E3D**, **L3D**).

## III. TIME EVOLUTIONS

Our study focuses on BS families for two values of the solitonic parameter,  $\sigma_0 = 0.08$  and  $\sigma_0 = 0.06$ ; the resulting BS models are displayed in the plane spanned by the central scalar amplitude  $A_0$  and the ADM mass  $M$  in Fig. 1. There we mark in orange color the ultracompact BSs possessing a pair of LRs; for both  $\sigma_0$  values, this set of UCOs extends to the left, beyond the global maximum of the  $M(A_0)$  curve, i.e. into the radially stable branch. This regime comprises the stars of interest in our study and we mark for each potential one representative specimen with properties as summarized in Table I. We begin our assessment of these two models by plotting in Fig. 2 the deviation  $\Delta A_0$  of the central

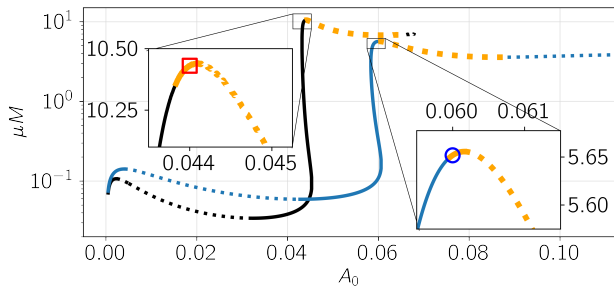


FIG. 1. The ADM mass is shown versus the central scalar-field amplitude  $A_0$  for the one-parameter families of BS models with solitonic potential parameter  $\sigma_0 = 0.06$  (black) and  $\sigma_0 = 0.08$  (blue). For each family solid (dashed) segments mark perturbatively stable (unstable) branches and we highlight in orange color BSs exhibiting a pair of LR. The insets indicate the perturbatively stable BH mimickers **S06A044** and **S08A06** that form the focus of our numerical investigation.

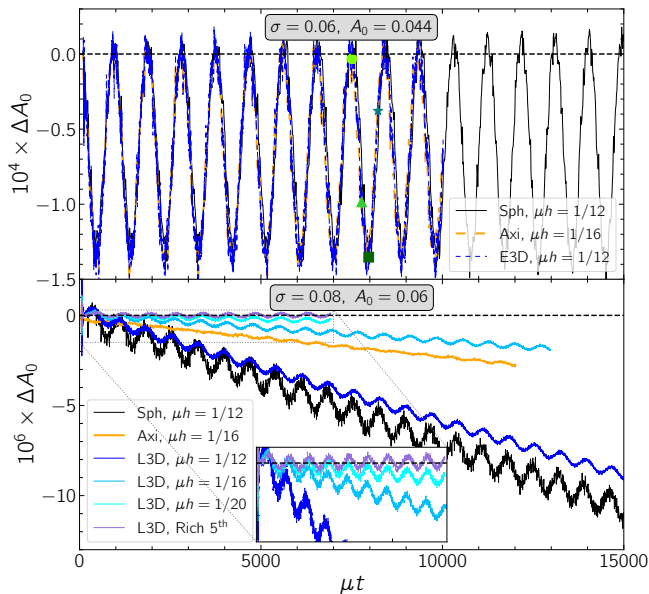


FIG. 2. Time evolution of the deviation  $\Delta A_0$  of the central scalar-field amplitude for the **S06A044** (top) and **S08A06** models (bottom) obtained in spherical symmetry, axi-symmetry and  $3D$ . The linear drift visible for **S08A06** converges away as shown in the inset. The four symbols in the top panel mark times when we evaluate the LR potential; cf. Fig. 4.

scalar-field amplitude from its initial value over time as obtained with different symmetry assumptions. For the **S06A044** model, we observe periodic oscillations with a relative magnitude  $\sim 0.3\%$  and good agreement by all codes. For **S08A06**, the oscillations are two orders of magnitude smaller and exhibit a linear drift which converges away with increasing resolution. This is demonstrated by the three blue-shaded curves obtained with L3D using different grid spacing  $h$ . Closer analysis of the differences yields 5<sup>th</sup>-order convergence and the Richardson extrapo-

lated function oscillates with high precision around zero.

Two features manifest in this figure require further explanation. First, we attribute the considerably larger oscillations observed for **S06A044** to a larger numerical error in the initial data; for this model, round-off uncertainty in the BS frequency  $\sim 10^{-32}$  can effect relative variations in the ADM mass or central lapse comparable to the level  $\Delta A_0/A_0$  observed. The **S08A06** model is less challenging and results in initial data with small uncertainty compared to those incurred in the time evolutions. This feature also explains the level of agreement between time evolutions employing different symmetry: the perturbations of **S06A044** are initial-data dominated with comparatively smaller contributions from the time evolution. For **S08A06**, on the other hand, details of the time evolution dominate, resulting in more pronounced relative – albeit tiny absolute – differences. This observation is confirmed by artificially lowering the quality of the initial data or time evolution which amplify drift or oscillation magnitude but with no change in frequency. The  $3D$  simulations displayed here have been computed using octant symmetry. We have performed additional versions of the  $3D$  simulations of **S08A06** using L3D (E3D) with  $h = 1/12$  in full grid mode up to  $t \gtrsim 3000$  ( $t \gtrsim 1000$ ); these give identical results to the octant runs within round-off precision.

The time evolution of the maximal Kretschmann scalar  $R^{\alpha\beta\gamma\delta}R_{\alpha\beta\gamma\delta}$  exhibits, up to an overall scaling, nearly identical behaviour as  $\Delta A_0$ , including the oscillatory pattern, drift and 5<sup>th</sup>-order convergence towards the equilibrium value. The Noether charge is conserved with identical convergence to within  $\Delta\mathcal{N}/\mathcal{N} \lesssim 10^{-3}$  and  $10^{-4}$  for **S06A044** and **S08A06**, respectively, predicting  $\Delta\mathcal{N}/\mathcal{N} \lesssim 10^{-6}$  in the continuum limit for **S08A06**. The constraints exhibit a rapid drop to  $L_2$  norms  $\sim 10^{-9}$  due to the CCZ4 damping [41], but converge only between 1<sup>st</sup> and 4<sup>th</sup> order.

#### IV. PERTURBATIVE PREDICTIONS

The oscillatory behaviour of  $\Delta A_0$  in Fig. 2 can be understood in terms of linearized calculations. For this purpose, we compute the frequency  $\chi_0$  of the fundamental radial oscillation mode for our BS families using the approach of Refs. [42, 43]; see App. C for details. The transitions between stable and unstable branches in Fig. 1 are characterized by zero crossings of  $\chi_0^2$  such that a real (imaginary)  $\chi_0$  implies radial (in)stability. For our BS models **S06A044** and **S08A06**, we obtain  $\chi_0^2 > 0$  as expected from their location on the rising slope of the  $M(A_0)$  curve. The behaviour of these BSs, as shown in Fig. 2, exhibits excellent agreement with the perturbative predictions: numerical imperfections trigger perturbations around the equilibrium solution whose time evolution is dominated by radial oscillations with the expected frequency. We quantify this agreement by plotting in Fig. 3 for **S08A06** the Fourier spectrum of  $\Delta A_0(t)$ ,

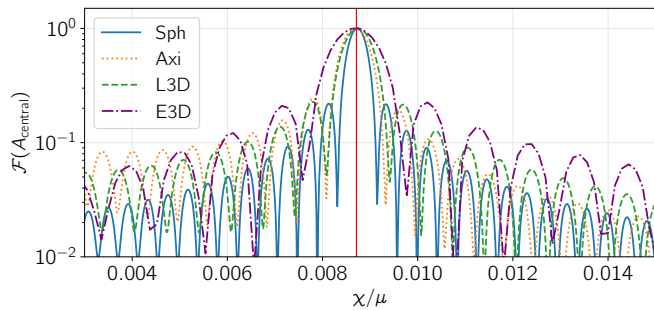


FIG. 3. Power spectrum of  $\Delta A_0(t)$  for S08A060; the red line marks the fundamental radial mode frequency  $\chi_0$ . Units on the vertical axis are arbitrary.

i.e. the data of Fig. 2. The spectrum peaks at the  $\chi_0$  value predicted by the perturbative calculation. The corresponding analysis for S06A044 yields similar agreement (see App. B).

## V. LIGHT-RING STRUCTURE

Having demonstrated the long-term stable behaviour of our BH mimickers S06A044 and S08A06, we now turn to the question whether their LR structure remains preserved. In a stationary and axisymmetric spacetime, a LR is defined as a null geodesic with a tangent vector field that is always a linear combination of the Killing vectors  $\partial_t$  and  $\partial_\phi$ , assuming coordinates  $(t, r, \theta, \phi)$  adapted to the symmetry. The conditions for a LR can then be recast as [15]

$$\partial_\mu H_\pm = 0, \quad H_\pm = \frac{-g_{t\phi} \pm \sqrt{g_{t\phi}^2 - g_{tt}g_{\phi\phi}}}{g_{\phi\phi}}, \quad (3)$$

and (un)stable LRs are located at local (maxima) minima of  $H_\pm$ . In spherical symmetry with adapted coordinates  $H_\pm$  simplifies to a single potential function  $H = \sqrt{-g_{tt}/g_{\phi\phi}}$ .

Under the assumption that an evolved spacetime remains nearly spherically symmetric and stationary, the potential function can be approximated by an *adiabatic effective potential* (AEP)  $H_{\text{eff}}$  computed via an averaging procedure analogous to Ref. [22]. Specifically, we transform between standard Cartesian and spherical coordinates  $x^\alpha = (t, x, y, z)$ ,  $\hat{x}^\mu = (t, R, \theta, \phi)$ . For a sphere of fixed coordinate radius  $R$ , we compute the proper area  $\mathcal{A}$ , the areal radius  $r := \sqrt{\mathcal{A}/(4\pi)}$ , and the AEP  $H_{\text{eff}}(r) = \sqrt{(\langle \alpha^2 \rangle - \langle \gamma_{ij} \beta^i \beta^j \rangle)}/r$ , where  $\alpha$ ,  $\beta^i$  and  $\gamma_{ij}$  are the lapse, shift and spatial metric in Cartesian coordinates, and  $\langle \cdot \rangle$  denotes averaging over the sphere. Repeating this procedure for a sequence of  $\sim 50$  coordinate spheres with  $\Delta R \approx 0.1$  across the relevant shell region, we obtain at each time  $t$  an estimate for the potential  $H_{\text{eff}}(r)$ . We validate the robustness of this method and the assumptions in App. D. Our analysis of the re-

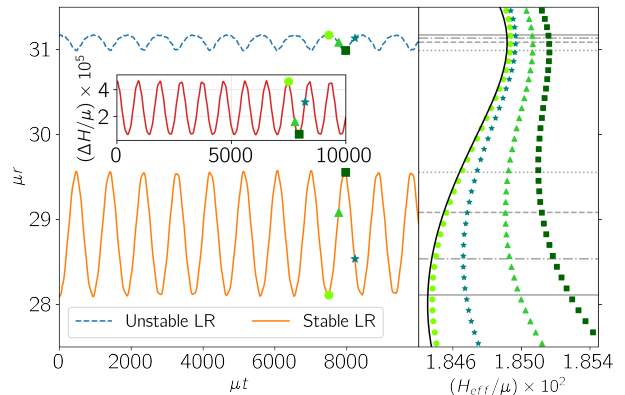


FIG. 4. (left) Areal radius of the (un)stable light ring over time, as extracted from the AEP  $H_{\text{eff}}$  (right) during the time evolution of S06A044 performed with E3D. The inset shows the difference between the extrema of the AEP over time. The green markers correspond to the snapshots of the AEP given in the right panel. The grey lines indicate the positions of the extrema. The solid line is the effective potential (3) at the start of the simulation.

sulting potentials for S06A044 and S08A06 indeed yields one minimum and one maximum at all  $t$ . The location of the respective LRs exhibits minor periodic variation commensurate with the BS oscillations observed in the other diagnostics, but the pair of light rings LRs remains in place with no indication of instability. We show these variations together with selected profiles of the AEP over a representative oscillation cycle in Fig. 4 for S06A044. The same behaviour, merely with smaller oscillation amplitude, is found for S08A06.

## VI. NON-LINEAR STABILITY

We complement our detailed analysis of the BS models S06A044 and S08A06 with a larger set of time evolutions of the  $\sigma = 0.08$  BS sequence. We have used all codes for this analysis but restrict 3D evolutions to  $\mu t \lesssim 3000$  for reasons of computational cost. In this analysis we define the instability time as the moment when  $A_0(t)$  departs by 10% from its equilibrium value. If  $A_0(t)$  yields no signature of departing from the oscillatory pattern seen in Fig. 2 within  $3000 \mu^{-1}$ , the model is designated stable. The result is shown in Fig. 5 and fully agrees with the perturbative predictions: models on unstable branches succumb to exponentially growing perturbations on a time scale that diverges at the threshold to stable branches. These transition points coincide with extrema in the  $M(A_0)$  curves, i.e. points where the oscillation frequency  $\chi_0$  of the fundamental mode switches between real and imaginary.

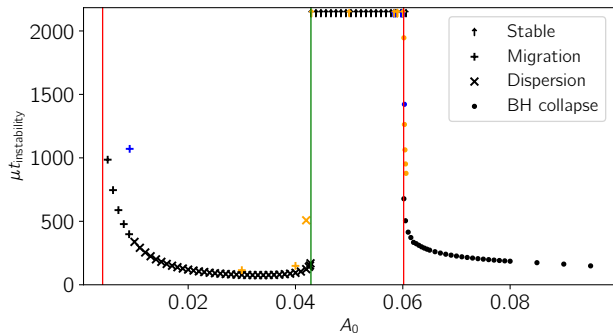


FIG. 5. Instability timescales as a function of  $A_0$  for solitonic BSs with  $\sigma_0 = 0.08$ . The vertical lines mark the transition between stable and unstable branches as predicted by linear theory; cf. Fig. 1. Marker style indicates dynamical fate while colour indicates code used: black is **Sph**, blue **Axi**, orange **L3D**. BS models whose time evolution show no sign of instability are represented with arrows at the top of the figure.

## VII. CONCLUDING REMARKS

We have performed a series of fully nonlinear evolutions of the Einstein-Klein-Gordon equations governing the dynamics of solitonic boson stars in the thin-shell regime in 3+1 dimensions imposing spherical, axi-, octant or no symmetry. A subset of the models under consideration are ultracompact, exhibiting a pair of light rings, one of which is stable. We have evolved these objects for  $\gtrsim 1000$  light crossing times, finding no evidence of an instability due to the appearance of the stable light ring, as previously conjectured [17, 21, 22]. We observe excellent agreement between the axisymmetric/3D evolutions and those in spherical symmetry, suggesting that the inclusion of nonspherical degrees of freedom does not significantly affect the stability of these models. Taking also into account the agreement of our numerical results with perturbative predictions for stability and fundamental radial oscillation frequencies, we interpret our findings as strong numerical evidence in favor of the stability of this class of BH mimickers.

As a cautionary note, we add that poor choices of numerical ingredients, in particular the constraint damping parameter  $\kappa_1$  of the CCZ4 formulation, can result in seemingly plausible instabilities of our thin-shell BSs. With  $M\kappa_1 \gg 0.1$ , for example, both models **S06A044** and **S08A06** collapse to a BH; the erroneous nature of these simulations reveals itself only through large and growing constraint violations and complete lack of convergence.

If the presence of the stable light ring is not sufficient to destroy these solitonic boson stars, this family of spherically symmetric models, as well as similar UCOs, can be considered as viable black hole mimickers again. The thin-shell solutions under consideration here can mimic the phenomenology of black holes in several different ways, as for example in the GW emission from binaries

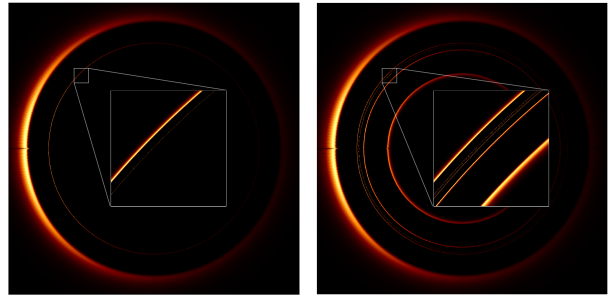


FIG. 6. Side-by-side comparison of ray-traced images of a (left) Schwarzschild BH and (right) the **S06A044** model of the same ADM mass. The color scale indicates the observed brightness intensity, in arbitrary units, from a simple geometrically thin disk located in the equatorial plane. Both panels also provide a zoom-in of the photon ring region, exhibiting their fractal structure. Images are obtained with **FOORT** [45, 46] - see App. E.

[14] or the creation of BH like shadows in VLBI images, [44]. Figure 6 illustrates how the **S06A044** model could resemble a Schwarzschild BH with the same ADM mass in the presence of an equatorial, optically thin accretion disk. The image of the BS clearly displays additional structure towards the center of the image, which is a result of the absence of a horizon as well as the pair of light rings. The outermost direct emission band, as well as the first lensed photon ring are nearly indistinguishable for both images.

## ACKNOWLEDGMENTS

G.A.M. is supported by the Cambridge Trust at the University of Cambridge. S.S. is supported by the Centre for Doctoral Training at the University of Cambridge funded through STFC. TE acknowledges Perimeter Institute for Theoretical Physics, supported by the Government of Canada through the Department of Innovation, Science and Economic Development and by the Province of Ontario through the Ministry of Colleges and Universities. This work has been supported by STFC Research Grant No. ST/V005669/1. We acknowledge support by the NSF Grant Nos. PHY-090003, PHY-1626190 and PHY-2110594, DiRAC projects ACTP284 and ACTP238, STFC capital Grants Nos. ST/P002307/1, ST/R002452/1, ST/I006285/1 and ST/V005618/1, STFC operations Grant No. ST/R00689X/1. Computations were done on the CSD3 and Fawcett (Cambridge), Cosma (Durham), Hawk (Cardiff), CIT LIGO Lab (Pasadena), Stampede2 (TACC) and Expanse (SDSC) clusters.

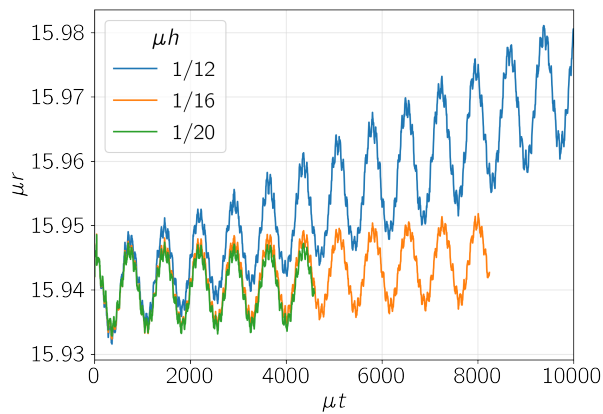


FIG. 7. Evolution of the areal radius of the stable LR for the S08A06 model obtained with the E3D code using different resolutions indicated in the legend. The differences between the curves yield convergence at 5<sup>th</sup> order.

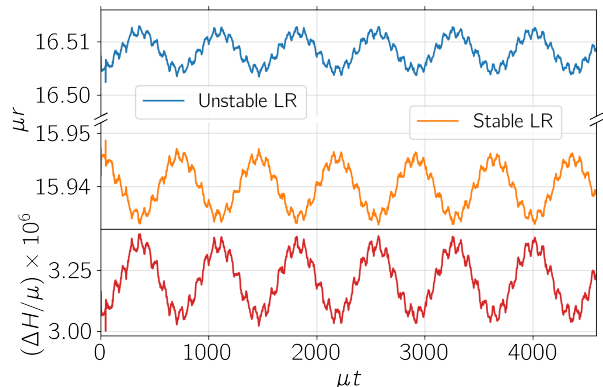


FIG. 8. Richardson extrapolation (5<sup>th</sup> order) of the LR areal radii of the S08A06 model based on the runs at resolutions  $\mu h = 1/16, 1/20$ . The bottom panel shows the evolution of the potential difference between the extrema of the AEP.

### Appendix A: Convergence Analysis

*Light rings:* We check convergence of the computed light ring (LR) radii for the S08A06 model by comparing results obtained at resolutions  $\mu h \in \{1/12, 1/16, 1/20\}$  and display in Fig. 7 the resulting areal radii of the stable LR as functions of time. At low resolution the LR radius exhibits a linear drift, much like what was observed for the central amplitude and Kretschmann scalar; cf. Fig. 2. Again, this drift converges away at 5<sup>th</sup> order, and the Richardson extrapolated values, obtained from the two highest-resolution runs and displayed in Fig. 8, oscillate around constant values.

For the S06A044 model, we observe no discernible drift and increasing the resolution merely results in convergence of the regular oscillations. Again, this underlines that the oscillatory perturbation of the S06A044 model is dominated by the quality of the initial data rather than details of the evolution.

*2D code:* We next discuss the convergence results for the S08A06 model obtained in axisymmetric evolutions with the Axi code. Using  $\mu h = 1/8$ ,  $\mu h = 1/12$  and  $\mu h = 1/16$  on the innermost refinement level for the low, medium and high resolutions, respectively, we obtain convergence between fourth and fifth order for the scalar field amplitude; cf. top panel of Fig. 9. In the bottom panels of the figure, we also monitor the volume-weighted  $L_2$  norms of the constraint violations. We find first-order convergence in the Hamiltonian constraint at very early times which gradually transitions to fourth order at  $\mu t \approx 20000$  and persists throughout the remainder of the simulation. The momentum constraint on the other hand rapidly reaches convergence between fourth and fifth order.

### Appendix B: Additional results for $\sigma_0 = 0.06$

In this section we present results for the  $\sigma_0 = 0.06$  family of models, supplementing those presented for  $\sigma_0 = 0.08$  above. In Fig. 10, we compare the power spectrum of central scalar-amplitude oscillations to the radial oscillation frequency, computed with perturbation theory. In this case the larger error in our initial data causes the system to migrate early on to a BS model with slightly smaller central scalar amplitude than the initial value  $A_0 = 0.044$ . Following Ref. [43] we take this effect into account by computing the radial frequency for a BS model with an amplitude averaged over several oscillation cycles,  $\langle A_0 \rangle = 0.04394$ . Once again, we find very good agreement between results from the perturbative analysis and the codes enforcing different symmetry assumptions.

In Fig. 11, we show timescales of instability for a sample of BS models with  $\sigma_0 = 0.06$ . As before, we define the instability timescale as the time at which the absolute change in the central amplitude  $|\Delta A_0(t)|$  exceeds 10% of the initial central amplitude  $\Delta A_0(0)$ . We find that the predictions of the radial perturbation theory are borne out by all codes regardless of symmetry assumptions. Models on the first unstable branch either migrate or disperse, and models on the second unstable branch always collapse to a BH. We emphasize that the actual timescales depend strongly on factors such as resolution, gauge, evolution method and parameter choices, mesh refinement, and other code differences; they should therefore only be interpreted as having a relative meaning. Note also that for some values of the central amplitude, multiple BS models exist; where ambiguous it is always the two lower-mass models which are stable, in accordance with the predictions of linear theory.

### Appendix C: Radial Oscillation Frequencies

In this section we discuss in detail the method used to compute fundamental radial oscillation frequencies for

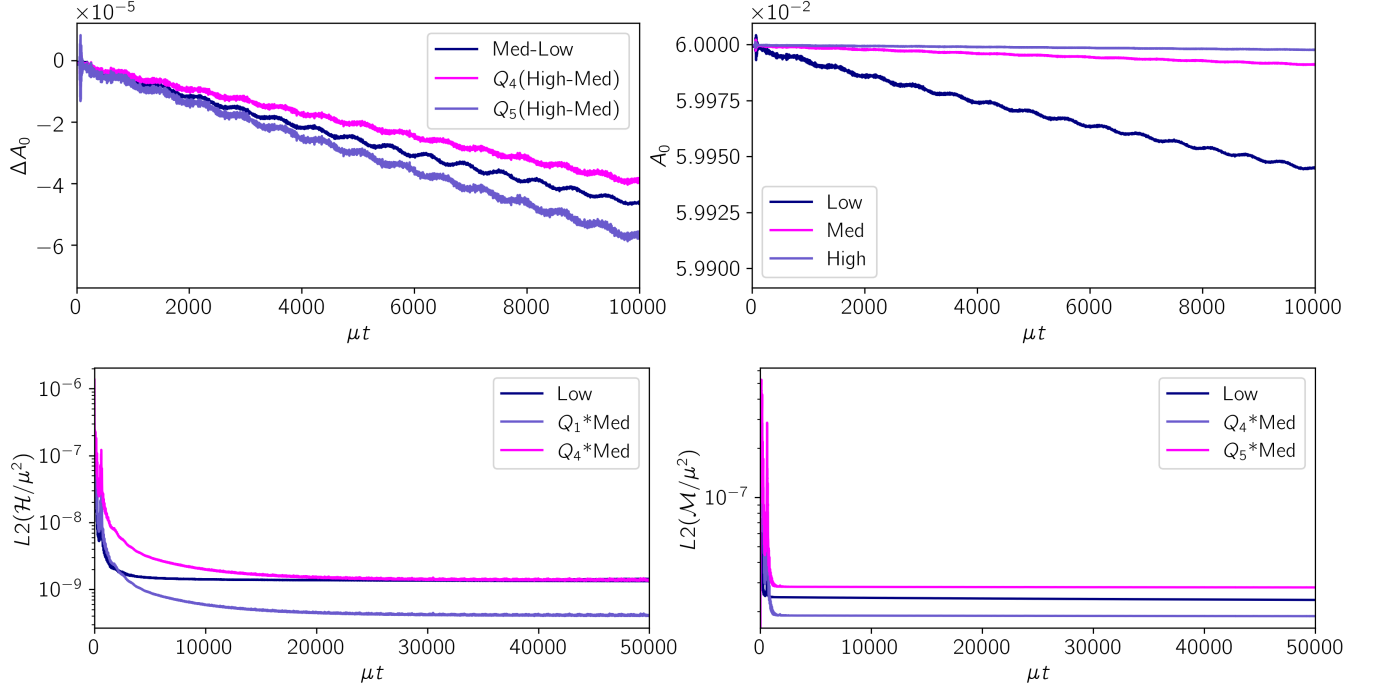


FIG. 9. Top (bottom) panels illustrate convergence results obtained from **Axi** simulations of the **S08A06** model for the scalar field amplitude (volume-weighted  $L_2$  norms of the Hamiltonian and momentum constraints). In the bottom panels we display the constraint violations for the low and medium resolutions and amplify the latter by factors  $Q_n$  as expected for  $n^{\text{th}}$ -order convergence.

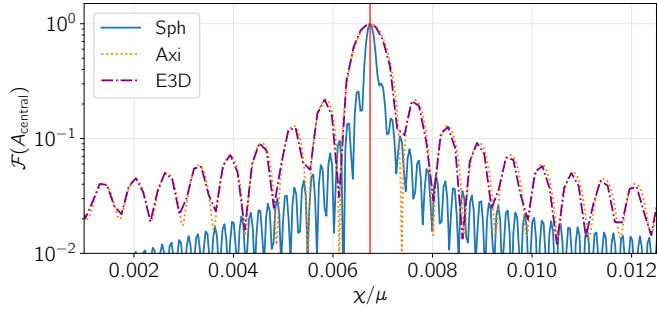


FIG. 10. Power spectrum of  $\Delta A_0(t)$  for **S06A044**; the red line marks the fundamental radial mode frequency  $\chi_0$ . Units on the vertical axis are arbitrary.

solitonic boson stars (BSs), presenting results across both stable branches for a variety of  $\sigma_0$ -values. In this section, we use overdots to denote time derivatives and primes to denote radial derivatives.

We begin with a spherically symmetric metric ansatz

$$ds^2 = -\alpha^2(t, r)dt^2 + X^2(t, r)dr^2 + r^2 d\Omega_2^2. \quad (\text{C1})$$

The Einstein field equations then reduce to the following,

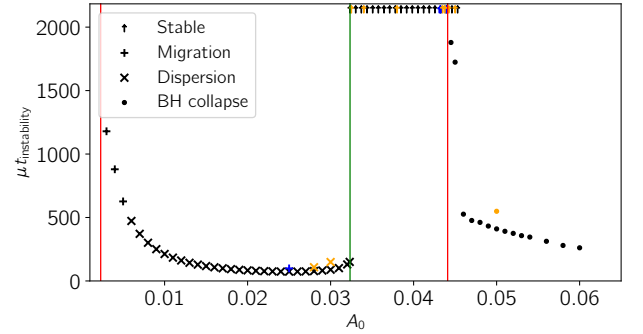


FIG. 11. Instability timescales as a function of  $A_0$  for solitonic BSs with  $\sigma_0 = 0.06$ . The vertical lines mark the transition between stable and unstable branches as predicted by linear theory. Marker style indicates dynamical fate while colour indicates code used: black is **Sph**, blue **Axi**, orange **E3D**. BS models whose time evolution show no sign of instability are represented with arrows at the top of the figure.

where we write  $\varphi(t, r) = \varphi_1 + i\varphi_2$  for real  $\varphi_1, \varphi_2$ ,

$$\frac{X'}{X} = \frac{1 - X^2}{2r} + 2\pi r X^2 \left( \frac{|\dot{\varphi}|^2}{\alpha^2} + \frac{|\varphi'|^2}{X^2} + V \right), \quad (\text{C2})$$

$$\frac{\dot{X}}{X} = 4\pi r (\dot{\varphi}_1 \varphi'_1 + \dot{\varphi}_2 \varphi'_2), \quad (\text{C3})$$

$$\frac{\alpha'}{\alpha} = -\frac{1 - X^2}{2r} + 2\pi r X^2 \left( \frac{|\dot{\varphi}|^2}{\alpha^2} + \frac{|\varphi'|^2}{X^2} - V \right), \quad (\text{C4})$$

$$\alpha'' = \frac{X\ddot{X}}{\alpha} - \frac{X\dot{X}\dot{\alpha}}{\alpha^2} + \frac{X'\alpha'}{X} - \frac{\alpha'}{r} + \frac{\alpha X'}{rX} + 4\pi\alpha \left( \frac{X^2}{\alpha^2} |\dot{\varphi}|^2 - |\varphi'|^2 - 4X^2 V \right). \quad (\text{C5})$$

Because of the Bianchi identities these equations are not independent. At first glance, one may be tempted to simply discard the final equation as a direct consequence of the former three, but later on Eq. (C5) turns out to be useful for converting the pulsation equations into a system of two second-order partial differential equations (PDEs) in two variables. The Einstein equations are complemented by the Klein-Gordon equation

$$\varphi_i'' = \left( \frac{X'}{X} - \frac{\alpha'}{\alpha} - \frac{2}{r} \right) \varphi_i' + \frac{X^2 \dot{\alpha} + X\alpha \dot{X}}{\alpha^3} \dot{\varphi}_i + \frac{X^2}{\alpha^2} \ddot{\varphi}_i \quad (\text{C6})$$

where  $i \in \{1, 2\}$ . Together, Eqs. (C2)-(C6) completely characterize our Einstein-Klein-Gordon system.

We now wish to expand around a background BS spacetime, particularizing at this point to the solitonic potential. For this purpose we introduce  $\delta\psi_1, \delta\psi_2, \delta\nu$  and  $\delta\lambda$  as perturbation functions of  $(t, r)$  according to

$$\begin{aligned} \varphi &= e^{i\omega t} (\psi_1 + i\psi_2), \\ \psi_1 &= A_0(r)(1 + \delta\psi_1), \quad \psi_2 = A_0(r)\delta\psi_2, \\ \alpha &= \alpha_0(r) \left( 1 + \frac{1}{2}\delta\nu \right), \quad X = X_0(r) \left( 1 + \frac{1}{2}\delta\lambda \right). \end{aligned} \quad (\text{C7})$$

At zeroth order in the perturbations, this yields the familiar ordinary-differential-equation (ODE) system for a stationary BS,

$$A_0'' = -\frac{\omega^2 X_0^2}{\alpha_0^2} A_0 + A_0' \left( \frac{X_0'}{X_0} - \frac{\alpha_0'}{\alpha_0} - \frac{2}{r} \right) + X_0^2 A_0 V'(A_0^2), \quad (\text{C8})$$

$$\frac{X_0'}{X_0} = \frac{1 - X_0^2}{2r} + 2\pi r \left[ (A_0')^2 + \frac{X_0^2}{\alpha_0^2} \omega^2 A_0^2 + X_0^2 V(A_0^2) \right], \quad (\text{C9})$$

$$\frac{\alpha_0'}{\alpha_0} = \frac{X_0^2 - 1}{2r} + 2\pi r \left[ (A_0')^2 + \frac{X_0^2}{\alpha_0^2} \omega^2 A_0^2 - X_0^2 V(A_0^2) \right]. \quad (\text{C10})$$

At linear order, after simplifying background terms by using Eqs. (C8), (C9) we obtain

$$\begin{aligned} \delta\psi_1'' &= X_0^2 \left( 1 - \frac{\omega^2}{\alpha_0^2} - \frac{8A_0^2}{\sigma_0^2} + \frac{12A_0^4}{\sigma_0^4} \right) \delta\lambda + \frac{X_0^2}{\alpha_0^2} \delta\dot{\psi}_1 + \frac{16A_0^2 X_0^2}{\sigma_0^2} \left( \frac{3A_0^2}{\sigma_0^2} - 1 \right) \delta\psi_1 + \frac{A_0'}{2A_0} (\delta\lambda' + 4\delta\psi_1' - \delta\nu') \\ &\quad + \frac{\omega X_0^2}{\alpha_0^2} (2\delta\dot{\psi}_2 - \omega\delta\nu) + \left( \frac{X_0'}{X_0} - \frac{\alpha_0'}{\alpha_0} - \frac{2}{r} \right) \delta\psi_1', \end{aligned} \quad (\text{C11})$$

$$\begin{aligned} \delta\lambda' &= \left( \frac{2X_0'}{X_0} - \frac{1}{r} - 4\pi r (A_0')^2 \right) \delta\lambda + 8\pi r X_0^2 \left( A_0^2 + \frac{(A_0')^2}{X_0^2} + \frac{\omega^2 A_0^2}{\alpha_0^2} + \frac{12A_0^6}{\sigma_0^4} - \frac{6A_0^4}{\sigma_0^2} \right) \delta\psi_1 \\ &\quad + \frac{4\pi r \omega A_0^2 X_0^2}{\alpha_0^2} (\omega\delta\nu + 2\delta\dot{\psi}_2) + 8\pi r A_0' A_0 \delta\psi_1'. \end{aligned} \quad (\text{C12})$$

$$\begin{aligned} \delta\ddot{\lambda} &= \frac{2\alpha_0}{X_0^2} \left[ \frac{\alpha_0 X_0'}{r X_0} + \alpha_0' \left( \frac{X_0'}{X_0} - \frac{1}{r} \right) - \alpha_0'' - 4\pi\alpha_0 (A_0')^2 \right] \delta\lambda - \frac{16\pi\alpha_0^2}{\omega X_0} \left[ \frac{(A_0')^2}{X_0^2} + A_0^2 - \frac{8A_0^4}{\sigma_0^2} + \frac{12A_0^6}{\sigma_0^4} - \omega^2 A_0^2 \right] \delta\psi_1 \\ &\quad + 8\pi\omega A_0^2 (\omega\delta\nu - 2\delta\dot{\psi}_2) + \frac{1}{r X_0} \left( \frac{r\alpha_0^2 \delta\nu'}{X_0} \right)' + \frac{16\pi\alpha_0^2 A_0' A_0}{X_0^2} \delta\psi_1' - \frac{1}{r X_0^2} (\alpha_0^2 + r\alpha_0\alpha_0') \delta\lambda'. \end{aligned} \quad (\text{C13})$$

Finally, it is convenient to also linearize the difference between Eqs. (C2) and (C4), which leads to

$$\begin{aligned} \delta\lambda' - \delta\nu' &= 2 \left( \frac{X_0'}{X_0} - \frac{\alpha_0'}{\alpha_0} - \frac{1}{r} \right) \\ &\quad + 16\pi r A_0^2 X_0^2 \left( 1 - \frac{8A_0^2}{\sigma_0^2} + \frac{12A_0^4}{\sigma_0^4} \right). \end{aligned} \quad (\text{C14})$$

Next, we make a harmonic ansatz  $\delta\psi_1(t, r) = e^{i\chi t} f(r)$ ,  $\delta\lambda(t, r) = e^{i\chi t} g(r)$  with  $\chi$  undetermined. The resulting system of two pulsation equations is self-adjoint, so that, in analogy to the BS frequencies  $\omega$ , the radial oscillation frequencies  $\chi$  form an infinite discrete sequence  $\chi_0^2 < \chi_1^2 < \dots$ , where the solution with eigenvalue  $\chi_n^2$  has  $n$  zero crossings in  $f$  and  $g$ . A negative  $\chi_0^2$  corresponds

to a radial instability, while  $\chi_0^2 > 0$  guarantees (linear) radial stability.

To obtain the first pulsation equation, we solve Eq. (C12) for  $\delta\psi_2$  and substitute into Eq. (C11) to obtain an equation that depends on  $\delta\nu$  only through its radial derivative which, in turn, can be removed using

$$f'' = X_0^2 \left[ 2 + \frac{2(A'_0)^2}{X_0^2 A_0^2} + \frac{2\omega^2 - \chi^2}{\alpha_0^2} + 8\pi r A_0 A'_0 - \frac{32A_0^2}{\sigma_0^2} (1 + 2\pi r A_0^2 A'_0) + \frac{8A_0^4}{\sigma_0^4} (9 + 12\pi r A_0 A'_0) \right] f \quad (\text{C15})$$

$$+ \left[ X_0^2 \left( 1 - \frac{8A_0^2}{\sigma_0^2} + \frac{12A_0^4}{\sigma_0^4} \right) - \frac{1}{4\pi r^2 A_0^2} - \frac{(A'_0)^2}{A_0^2} - \frac{A'_0}{r A_0} - \frac{A'_0 \alpha'_0}{A_0 \alpha_0} + \frac{X'_0}{X_0 A_0} \left( A'_0 + \frac{1}{2\pi r A_0} \right) \right] g$$

$$+ \left( \frac{X'_0}{X_0} - \frac{\alpha'_0}{\alpha_0} - \frac{2}{r} \right) f' - \frac{1}{4\pi r A_0^2} g',$$

$$g'' = 32\pi r X_0^2 \left[ A_0 A'_0 + \frac{\alpha'_0 A_0^2}{\alpha_0} - \frac{8A_0^3}{\sigma_0^2} \left( 2A'_0 + \frac{A_0 \alpha'_0}{\alpha_0} \right) + \frac{X'_0}{X_0} \left( A_0^2 - \frac{4A_0^4}{\sigma_0^2} + \frac{6A_0^6}{\sigma_0^4} - \frac{(A'_0)^2}{X_0^2} \right) \right] f \quad (\text{C16})$$

$$+ \frac{12A_0^5}{\sigma_0^4} \left( 3A'_0 + \frac{A_0 \alpha'_0}{\alpha_0} \right) \Big] f + 3 \left( \frac{X'_0}{X_0} - \frac{\alpha'_0}{\alpha_0} \right) g' + \left[ 16\pi (A'_0)^2 - \frac{\chi^2 X_0^2 - 2(\alpha'_0)^2}{\alpha_0^2} - \frac{4\alpha'_0}{r \alpha_0} + \frac{2}{r^2} \right. \\ \left. + \frac{2}{X_0} \left( X_0'' + \frac{2\alpha'_0 X'_0}{\alpha_0} - \frac{2(X'_0)^2}{X_0} - \frac{X'_0}{r} \right) \right] g + 16\pi r X_0^2 A_0^2 \left( 1 - \frac{8A_0^2}{\sigma_0^2} + \frac{12A_0^4}{\sigma_0^4} - 2\frac{A_0 A'_0}{r X_0^2} \right) f'.$$

Before we can solve this system numerically, we must determine its behavior in the limit  $r \rightarrow 0$ . Bearing in mind the even parity of scalar functions across  $r = 0$  and using our freedom to rescale the perturbations, we can expand them without loss of generality as  $f = 1 + \frac{\alpha}{2}r^2 + \mathcal{O}(r^4)$  and  $g = \beta + \frac{\gamma}{2}r^2 + \mathcal{O}(r^4)$ . Inserting into Eqs. (C15) and (C16) gives us

$$a = \frac{1}{3} \left( 2 + \frac{2\omega^2 - \chi^2}{\alpha_0(0)^2} - \frac{32A_0(0)^2}{\sigma_0^2} + \frac{72A_0(0)^4}{\sigma_0^4} \right) - \frac{\gamma}{8\pi A_0(0)^2}, \quad (\text{C17})$$

as well as  $\beta = 0$  at leading order. There is a degeneracy, however, at the following order so that  $\gamma$  remains undetermined. In consequence, we have *two* undetermined parameters,  $\chi$  and  $\gamma$ , which we solve for using a shooting method.

To do this, we need two appropriate boundary conditions at  $r \rightarrow \infty$ . Asymptotic flatness requires that  $\delta\lambda$  vanishes at infinity. The second condition is obtained by enforcing that the perturbation conserves the Noether charge

$$\mathcal{N} = \int \sqrt{-\det g} J^0 d^3x, \quad J^\mu = \frac{i}{2} g^{\mu\nu} (\bar{\varphi} \partial_\nu \varphi - \varphi \partial_\nu \bar{\varphi}),$$

compliant with the scalar field's  $U(1)$  symmetry. The

(C14). For the second pulsation equation, we combine Eqs. (C13), (C12) and (C8) to obtain an equation that depends on  $\delta\nu'$  and  $\delta\nu''$  but not  $\delta\nu$  directly. By using Eq. (C14), its derivative and Eq. (C8), we can eliminate  $\delta\nu$  completely and thus arrive at our final system of two ODEs,

variation in the Noether charge is given by

$$\delta\mathcal{N} = 4\pi \int_0^\infty \frac{A_0^2 r^2}{\alpha_0} dr \left[ \omega X_0 (\delta\lambda - \delta\nu) + 2\delta\psi_2 + 4\omega\delta\psi_1 \right] \quad (\text{C18})$$

Combining with Eq. (C12) allows us to eliminate  $\delta\nu$  whence, using the background equations (C8)-(C10), we can write the integrand as a total derivative and find

$$\delta\mathcal{N} = \frac{1}{\omega X_0} (8\pi r^2 \alpha_0 A_0 A'_0 f - r \alpha_0 g) \Big|_{r=0}^\infty. \quad (\text{C19})$$

Despite appearances, the first term is nonnegligible in this expression due to the exponential behavior of  $f$  which vanishes only for precise choices of the shooting parameters  $\chi$  and  $\gamma$ . Thus, for regular perturbations which remain finite at  $r = 0$ , the condition  $\delta\mathcal{N} = 0$  supplies a second boundary condition at infinity.

Finally, it is worth noting that because  $\delta\lambda$  is related to the perturbation to the total mass according to

$$\delta\lambda = \frac{2X_0^2}{r} \delta M, \quad (\text{C20})$$

at large radius, our two conditions amount to enforcing that both the mass and particle number of the BS are unchanged by the perturbation. In practice, we solve Eqs. (C15) and (C16) using a standard fourth-order Runge-Kutta method, shooting for the undetermined values  $\chi$  and  $\gamma$  for each model. We determine these two parameters using a bisection method similar to that commonly used to determine the frequency  $\omega$  for equilibrium

BS models. Interestingly, we encounter the same challenging accuracy requirements in our determination of  $\chi$  and  $\gamma$  for thin-shell BSs as observed when calculating the BS frequency  $\omega$ ; therefore, we also compute the radial oscillation spectrum using quadruple precision.

In this work, we restrict our attention to presenting positive  $\chi_0^2$  values corresponding to radially stable models, though this approach can be used to compute negative values as well as higher-order oscillation frequencies. The point in the BS parameter space at which models transition from stable to unstable is marked by the existence of a zero-frequency perturbation,  $\chi_0^2 = 0$ . Such zero-frequency perturbations can only exist where there are two neighboring solutions with the same mass (or equivalently, particle number). Therefore, the condition  $dM/dA(0) = 0$  is a necessary but insufficient criterion for the transition of a radial oscillation mode from stability to instability. For mini BSs, only models with smaller central amplitude than that corresponding to the maximum mass model are stable [42]. There is hence only a single stable branch for mini BSs. However, for solitonic models with sufficiently small  $\sigma_0$ , a second stable branch emerges; see e.g. Fig. 4 in Ref. [47] for representative examples.

In Fig. 12, we present values of  $\chi_0^2$  for mini and solitonic BS models on both stable branches. Our results confirm the radial stability of solitonic BS models on the second stable branch, including in the thin-shell regime where  $M$  and  $\omega$  become multi-valued functions of the central amplitude

Indeed, we see that the curve of  $\chi_0^2$  against the central amplitude also becomes multivalued for these  $\sigma_0$ -values, and in fact self-intersects. In the case of mini BSs, our results are compatible with those computed in Ref. [43], while the solitonic results are verified by comparing to the power spectrums of dynamical evolutions.

#### Appendix D: Adiabatic Effective Potential

To assess whether the BS remains ultracompact throughout the evolution, we need to check whether light rings persist. As the BS is evolved in 3+1 dimensions, the spacetime generally loses the spherical symmetry as a result of numerical errors and gauge effects that excite asymmetric modes. In terms of the 3+1 metric

$$ds^2 = -\alpha^2 dt^2 + \gamma_{ij} (dx^i + \beta^i dt) (dx^j + \beta^j dt), \quad (\text{D1})$$

where  $\alpha$ ,  $\beta^i$  and  $\gamma_{ij}$  are the standard lapse, shift and spatial metric, this means that the shift will become non-zero, and the spatial metric will deviate from spherical symmetry. In principle, the effective potential in the form

$$H(r, \theta) = \sqrt{\frac{-g_{tt}}{g_{\phi\phi}}} \quad (\text{D2})$$

is only defined for stationary spacetimes that exhibit spherical symmetry, whose metric components we hence-

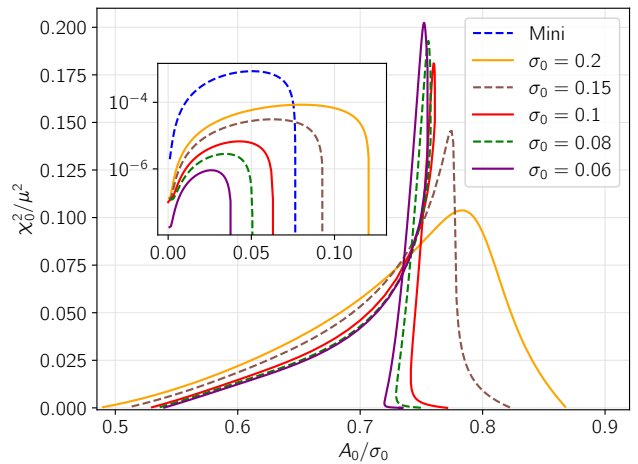


FIG. 12. Fundamental radial oscillation frequencies  $\chi_0^2$  against central amplitude  $A_0$  for mini and solitonic BSs with a variety of  $\sigma_0$ -values. The main figure shows the second stable branch, while the inset shows the first. Central amplitudes are rescaled by the appropriate  $\sigma_0$ -value, apart from mini BSs, which undergo no rescaling.

forth denote  $g_{\alpha\beta}$  in this section. Given that our evolutions are expected to approximately respect the symmetries of the initial data, the presence of (stable) bound geodesics can still be deduced from the Adiabatic Effective Potential (AEP).

We adapt the approach of Ref. [22] from (approximate) axisymmetry to our spherically symmetric setting. Under the assumptions outlined in this work, the metric component  $g_{tt}$  in the effective potential (D2) can be replaced by the evolution variables according to

$$g_{tt} \rightarrow -\langle \alpha^2 \rangle + \langle \gamma_{ij} \beta^i \beta^j \rangle, \quad (\text{D3})$$

where the brackets denote averaging over a sphere of fixed coordinate radius  $R = \sqrt{x^2 + y^2 + z^2}$  and  $x, y, z$  are the Cartesian coordinates of the evolution grid. We convert  $R$  into the areal radius through [48]

$$r^2 = \frac{\mathcal{A}}{4\pi} = \frac{1}{4\pi} \langle \sqrt{\det q} \rangle \quad (\text{D4})$$

where  $q$  is the metric induced on the sphere  $R = \text{const.}$  Mapping the Cartesian evolution coordinates  $(x, y, z)$  to angular coordinates  $(R, \tilde{\theta}, \tilde{\phi})$  according to

$$x = R \sin \tilde{\theta} \cos \tilde{\phi}, \quad y = R \sin \tilde{\theta} \sin \tilde{\phi}, \quad z = R \cos \tilde{\theta},$$

we can express the induced metric as

$$\begin{aligned} q_{\tilde{\theta}\tilde{\theta}} &= z^2 (\gamma_{xx} \cos^2 \tilde{\phi} + \gamma_{yy} \sin^2 \tilde{\phi}) + \gamma_{zz} R^2 \sin^2 \tilde{\theta} \\ &\quad + \gamma_{xy} z^2 \sin(2\tilde{\phi}) - 2zR \sin \tilde{\theta} (\gamma_{xz} \cos \tilde{\phi} + \gamma_{yz} \sin \tilde{\phi}), \\ q_{\tilde{\phi}\tilde{\phi}} &= \gamma_{xx} y^2 - 2\gamma_{xy} xy + \gamma_{yy} x^2, \\ q_{\tilde{\theta}\tilde{\phi}} &= \gamma_{yy} xz \sin \tilde{\phi} - \gamma_{xx} yz \cos \tilde{\phi} + \gamma_{xy} z (x \cos \tilde{\phi} - y \sin \tilde{\phi}) \\ &\quad + R \sin \tilde{\theta} (\gamma_{xz} y - \gamma_{yz} x). \end{aligned}$$

In the equatorial plane  $\theta = \frac{\pi}{2}$  of the stationary and spherically symmetric spacetime, we have  $g_{\phi\phi} = r^2$ . Replacing  $g_{\phi\phi} \rightarrow \frac{1}{4\pi} \langle \sqrt{\det q} \rangle$  and using Eqs. (D2)-(D4) we now define the AEP as

$$H_{\text{eff}}(R) = \sqrt{\frac{\langle \alpha^2 \rangle - \langle \gamma_{ij} \beta^i \beta^j \rangle}{\langle \sqrt{\det q} \rangle / 4\pi}}, \quad (\text{D5})$$

which is straightforwardly translated into a function of areal radius using Eq. (D4). In the idealized case where our simulation is perfectly spherically symmetric and stationary, Eq. (D5) reduces to Eq. (D2). As long as this AEP has extrema we have evidence that the BS is still ultracompact, featuring a pair of (perturbed) light rings. In practice, the AEP is extracted at a number of coordinate radii with resolution  $\Delta R \approx 0.1$  in the range where we expect the light rings to be.

In order to quantify the deviation from spherical symmetry, we compute the variation of the relevant quantities over the extraction spheres. For this purpose, we define the relative standard deviation of a variable  $X$  as

$$\delta(X) \equiv \frac{\sigma(X)}{\langle X \rangle} \equiv \frac{\sqrt{\langle (X - \langle X \rangle)^2 \rangle}}{\langle X \rangle}, \quad (\text{D6})$$

where  $\langle X \rangle$  denotes the average over the coordinate sphere with radius  $R$ . Figure 13 shows the relative standard deviation for the individual terms of Eq. (D5), as well as that of the AEP itself, as obtained for 192 points on each sphere.

In the case of  $\beta^2 \equiv \gamma_{ij} \beta^i \beta^j$  we have  $\delta(\beta^2) \gtrsim 10^{-2}$ , reaching order unity at certain times. This relatively large  $\delta(\beta^2)$  is merely due to the shift vector having a very small norm. This is further underlined by the ratio  $\langle \beta^2 \rangle / \langle \alpha^2 \rangle \lesssim 10^{-9}$ . For the other variables, the relative standard deviation is  $\lesssim 10^{-6}$ , suggesting that the spacetime is very close to spherical symmetry and approximately stationary.

In order to investigate whether these variations influence the conclusion about the presence of light rings, we plot  $\sigma(H_{\text{eff}})/\Delta H$ , where  $\Delta H$  is the potential difference between the extracted extrema of the AEP. This value varies around  $\sim 10^{-3} - 10^{-2}$ , implying that the deviations from our symmetry assumptions explain at most 1% of the observed potential difference between the extrema, demonstrating their robustness.

The conclusions for S06A044 are similar and displayed in Fig. 14. The major difference is that the norm of the shift vector compared to the lapse is comparatively larger at  $\langle \beta^2 \rangle / \langle \alpha^2 \rangle \sim 10^{-6}$ . This is due to the larger dynamics in this more challenging simulation, as was apparent from other diagnostics. The ratio  $\sigma(H_{\text{eff}})/\Delta H \lesssim 10^{-3}$  is smaller by an order of magnitude, an artifact of the more pronounced extrema for this more extreme model.

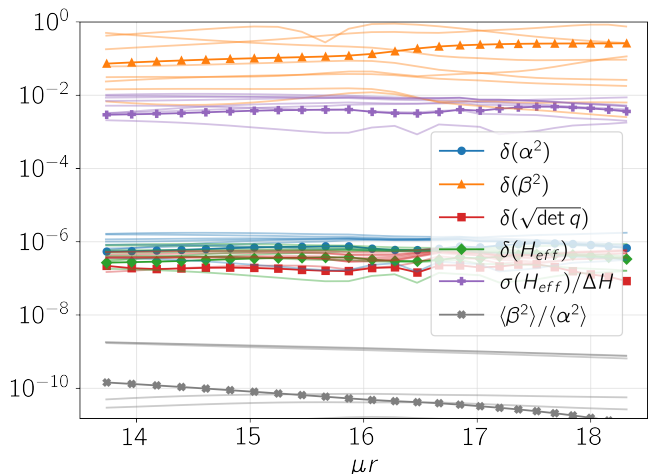


FIG. 13. Diagnostics to assess the deviations from spherical symmetry and stationarity for BS model S08A006. Brackets denote averaging over an extraction sphere, whereas  $\sigma$  denotes the standard deviation with respect to this average value. The relative standard deviation is  $\delta(X) \equiv \sigma(X)/\langle X \rangle$ , and  $\Delta H$  denotes the potential difference between the two extrema of the AEP. The lines with markers correspond to time  $\mu t = 75$ , after the initial dynamics start to settle down. The other lines correspond to extractions at later times ( $\mu t \in \{250, 500, \dots, 2000\}$ ) to illustrate that the conclusions also hold at later times.

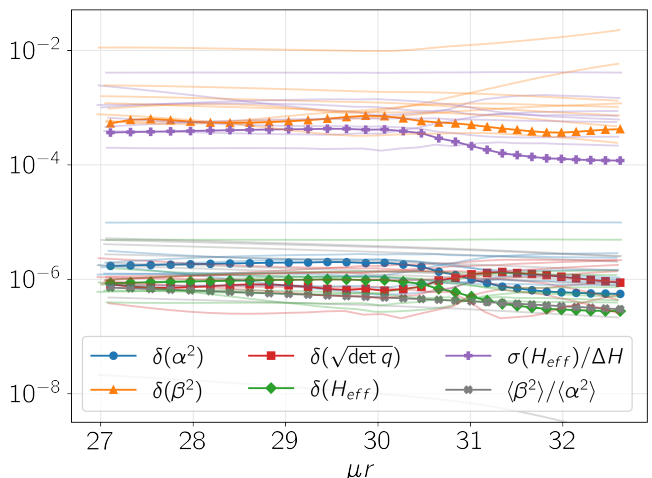


FIG. 14. Same as Fig. 13, but for BS model S06A044.

## Appendix E: Ray tracing

The ray-traced images are obtained using FOORT, a Flexible Object-Oriented Ray Tracer that is publicly available on GitHub [45, 46]. The geodesic equations are integrated using the Verlet scheme in order to produce images of a variety of spacetimes. It is highly flexible and easily accommodates new analytical or numerical spacetimes, such as a boson star. It employs adaptive mesh refinement. The images in the main text are produced

assuming an optically thin equatorial disk with emission profile given by

$$I_0(r) = ((r - \rho)^2 + \Delta^2)^{-1/2} \times \exp\left(-\frac{1}{2} \left[ \kappa + \operatorname{arcsinh}\left(\frac{r - \rho}{\Delta}\right) \right]^2\right), \quad (\text{E1})$$

a simple analytical model proposed in Ref. [49]. The parameters used are  $(\rho, \Delta, \kappa) = (60, 2.5, -2)$ , with the

first value corresponding to  $\sim 6M$ , the radial coordinate of the ISCO in Schwarzschild spacetime. Although the spacetime is non-rotating, the fluid velocity can be modeled with a mix of radial and (sub)Keplerian orbits, as described in e.g. Refs. [50, 51]. For the images in the main text, parameters  $\xi = \beta_r = \beta_\phi = 1.0$  in the conventions of Ref. [51] have been used, corresponding to pure Keplerian orbits which give rise to the observed asymmetry in the images.

- 
- [1] S. Bowyer, E. T. Byram, T. A. Chubb, and H. Friedmann, *Science* **147**, 394 (1965).
- [2] C. Hazard, M. B. Mackey, and A. J. Shimmins, *Nature* **197**, 1037 (1963).
- [3] M. Schmidt, *Nature* **197**, 1040 (1963).
- [4] B. P. Abbott *et al.*, *Phys. Rev. Lett.* **116**, 061102 (2016), arXiv:1602.03837 [gr-qc].
- [5] R. Abbott *et al.* (KAGRA, VIRGO, LIGO Scientific), *Phys. Rev. X* **13**, 041039 (2023), arXiv:2111.03606 [gr-qc].
- [6] R. Abbott *et al.* (LIGO Scientific, VIRGO, KAGRA), (2021), arXiv:2112.06861 [gr-qc].
- [7] K. Akiyama *et al.* (Event Horizon Telescope), *Astrophys. J. Lett.* **875**, L1 (2019), arXiv:1906.11238 [astro-ph.GA].
- [8] K. Akiyama *et al.* (Event Horizon Telescope), *Astrophys. J. Lett.* **930**, L12 (2022), arXiv:2311.08680 [astro-ph.HE].
- [9] J. L. Synge, *Mon. Not. Roy. Astron. Soc.* **131**, 463 (1966).
- [10] V. Cardoso, A. S. Miranda, E. Berti, H. Witek, and V. T. Zanchin, *Phys. Rev. D* **79**, 064016 (2009), arXiv:0812.1806 [hep-th].
- [11] Y. Koga, N. Asaka, M. Kimura, and K. Okabayashi, *Phys. Rev. D* **105**, 104040 (2022), arXiv:2202.00201 [gr-qc].
- [12] S. H. Völkel, N. Franchini, E. Barausse, and E. Berti, *Phys. Rev. D* **106**, 124036 (2022), arXiv:2209.10564 [gr-qc].
- [13] S. D. Mathur, *Classical and Quantum Gravity* **26**, 224001 (2009).
- [14] T. Evstafyeva, U. Sperhake, I. Romero-Shaw, and M. Agathos, *Phys. Rev. Lett.* **133**, 131401 (2024), arXiv:2406.02715 [gr-qc], arXiv:2406.02715 [gr-qc].
- [15] P. V. P. Cunha, E. Berti, and C. A. R. Herdeiro, *Phys. Rev. Lett.* **119**, 251102 (2017), arXiv:1708.04211 [gr-qc].
- [16] P. V. P. Cunha and C. A. R. Herdeiro, *Phys. Rev. Lett.* **124**, 181101 (2020), arXiv:2003.06445 [gr-qc].
- [17] J. Keir, *Class. Quant. Grav.* **33**, 135009 (2016), arXiv:1404.7036 [gr-qc].
- [18] P. Bizoń and A. Rostworowski, *Phys. Rev. Lett.* **107**, 031102 (2011), arXiv:1104.3702 [gr-qc].
- [19] G. Holzegel and J. Smulevici, *Commun. Pure Appl. Math.* **66**, 1751 (2013), arXiv:1110.6794 [gr-qc].
- [20] G. Holzegel and J. Smulevici, *Anal. Part. Diff. Eq.* **7**, 1057 (2014), arXiv:1303.5944 [gr-qc].
- [21] V. Cardoso, L. C. B. Crispino, C. F. B. Macedo, H. Okawa, and P. Pani, *Phys. Rev. D* **90**, 044069 (2014), arXiv:1406.5510 [gr-qc].
- [22] P. V. P. Cunha, C. Herdeiro, E. Radu, and N. Sanchis-Gual, *Phys. Rev. Lett.* **130**, 061401 (2023), arXiv:2207.13713 [gr-qc].
- [23] P. V. P. Cunha, (2025), arXiv:2503.00117 [gr-qc].
- [24] N. Siemonsen, *Phys. Rev. Lett.* **133**, 031401 (2024), arXiv:2404.14536 [gr-qc].
- [25] G. Guo, P. Wang, and Y. Zhang, (2024), arXiv:2403.02089 [gr-qc].
- [26] G. Benomio, A. Cárdenas-Avendaño, F. Pretorius, and A. Sullivan, (2024), arXiv:2411.17445 [gr-qc].
- [27] J. Redondo-Yuste and A. Cárdenas-Avendaño, (2025), arXiv:2502.18643 [gr-qc].
- [28] L. G. Collodel and D. D. Doneva, *Phys. Rev. D* **106**, 084057 (2022), arXiv:2203.08203 [gr-qc].
- [29] T. Evstafyeva, R. Rosca-Mead, U. Sperhake, and B. Bruegmann, *Phys. Rev. D* **108**, 104064 (2023), arXiv:2310.05200 [gr-qc].
- [30] T. W. Baumgarte and S. L. Shapiro, *Phys. Rev. D* **59**, 024007 (1998), gr-qc/9810065.
- [31] M. Shibata and T. Nakamura, *Phys. Rev. D* **52**, 5428 (1995).
- [32] D. Alic, C. Bona-Casas, C. Bona, L. Rezzolla, and C. Palenzuela, *Phys. Rev. D* **85**, 064040 (2012), arXiv:1106.2254 [gr-qc].
- [33] W. G. Cook, P. Figueras, M. Kunesch, U. Sperhake, and S. Tunyasuvunakool, *Int. J. Mod. Phys. D* **25**, 1641013 (2016), arXiv:1603.00362 [gr-qc].
- [34] “ExoZvezda code,” GitHub repository (2024).
- [35] M. Radia, U. Sperhake, A. Drew, K. Clough, P. Figueras, E. A. Lim, J. L. Ripley, J. C. Aurrekoetxea, T. França, and T. Helfer, *Class. Quant. Grav.* **39**, 135006 (2022), arXiv:2112.10567 [gr-qc].
- [36] T. Andrade *et al.*, *J. Open Source Softw.* **6**, 3703 (2021), arXiv:2201.03458 [gr-qc].
- [37] M. Adams *et al.*, *Chombo Software Package for AMR Applications - Design Document*, Tech. Rep. LBNL-6616E (Lawrence Berkeley National Laboratory, 2019).
- [38] U. Sperhake, *Phys. Rev. D* **76**, 104015 (2007), gr-qc/0606079.
- [39] Allen, G. and Goodale, T. and Massó, J. and Seidel, E., in *Proceedings of Eighth IEEE International Symposium on High Performance Distributed Computing, HPDC-8, Redondo Beach, 1999* (IEEE Press, Piscataway, New Jersey, United States, 1999).
- [40] E. Schnetter, S. H. Hawley, and I. Hawke, *Class. Quant. Grav.* **21**, 1465 (2004), gr-qc/0310042.
- [41] D. Alic, W. Kastaun, and L. Rezzolla, *Phys. Rev. D* **88**, 064049 (2013), arXiv:1307.7391 [gr-qc].
- [42] M. Gleiser and R. Watkins, *Nucl. Phys. B* **319**, 733 (1989).
- [43] B. Kain, *Phys. Rev. D* **103**, 123003 (2021), arXiv:2106.01740 [gr-qc].

- [44] J. L. Rosa, C. F. B. Macedo, and D. Rubiera-Garcia, *Phys. Rev. D* **108**, 044021 (2023), arXiv:2303.17296 [gr-qc].
- [45] D. R. Mayerson, “FOORT: Flexible Object-Oriented Ray Tracing,” (2024).
- [46] D. R. Mayerson, F. Bacchini, and S. J. Staelens, (unpublished).
- [47] B.-X. Ge, E. A. Lim, U. Sperhake, T. Evstafyeva, D. Cors, E. de Jong, R. Croft, and T. Helfer, (2024), arXiv:2410.23839 [gr-qc].
- [48] Note that it is not guaranteed that the coordinate sphere actually corresponds to a sphere in terms of the areal radius. Again, if the evolution remains sufficiently close to spherical symmetry, this is a good approximation.
- [49] S. E. Gralla, A. Lupsasca, and D. P. Marrone, *Physical Review D* **102**, 124004 (2020).
- [50] H.-Y. Pu, K. Akiyama, and K. Asada, *The Astrophysical Journal* **831**, 4 (2016).
- [51] A. Cárdenas-Avendaño, A. Lupsasca, and H. Zhu, *Phys. Rev. D* **107**, 043030 (2023).